Computer Methods in Applied Mechanics and Engineering 433 (2025) 117501

Contents lists available at ScienceDirect

Comput. Methods Appl. Mech. Engrg.

journal homepage: www.elsevier.com/locate/cma

GDSW preconditioners for composite Discontinuous Galerkin discretizations of multicompartment reaction–diffusion problems

Ngoc Mai Monica Huynh [a,*], Luca F. Pavarino [a], Simone Scacchi [b]

[a] Department of Mathematics, University of Pavia, via Ferrata 1, Pavia, 27100, Italy
[b] Department of Mathematics, University of Milano, via Saldini 50, Milano, 20133, Italy

ARTICLE INFO

MSC:
65N55
65M55
65F10
92C30

Keywords:
Cardiac cell-by-cell models
Composite Discontinuous Galerkin methods
Scalable Domain Decomposition methods
BDDC preconditioners

ABSTRACT

The aim of the present work is to design, analyze theoretically, and test numerically, a generalized Dryja–Smith–Widlund (GDSW) preconditioner for composite Discontinuous Galerkin discretizations of multicompartment parabolic reaction–diffusion equations, where the solution can exhibit natural discontinuities across the domain. We prove that the resulting preconditioned operator for the solution of the discrete system arising at each time step converges with a scalable and quasi-optimal upper bound for the condition number. The GDSW preconditioner is then applied to the EMI (Extracellular - Membrane - Intracellular) reaction–diffusion system, recently proposed to model microscopically the spatiotemporal evolution of cardiac bioelectrical potentials. Numerical tests validate the scalability and quasi-optimality of the EMI-GDSW preconditioner, and investigate its robustness with respect to the time-step size as well as jumps in the diffusion coefficients.

1. Introduction

In the present work, we construct and analyze a generalized Dryja–Smith–Widlund preconditioner for parabolic reaction–diffusion problems where the equations present a low-order term that can lead to discontinuities in the solution on the considered domain. Such problems arise in many applications, such as microscopic modeling in biomechanics, porous media [1,2], and cardiac and excitable tissue modeling [3–5], where the low-order term represents a 3D-1D (or 3D-0D) poroelasticity network or couples diffusive phenomena with microscopic ionic exchanges among cells. The numerical simulation of these phenomena presents challenges because of the different physics and scales involved, which require spatial and time discretizations that lead to matrix problems with very large dimensions. Common choices for space discretization are based on discontinuous Galerkin (DG) methods (see [1,6]), which usually need to be coupled with efficient preconditioned solvers in order to tackle their computational complexity.

In the context of DG discretizations, several solvers have been proposed, ranging from block preconditioners [7] (which can be tailored to each specific physics in the case of coupled problems) to two-level methods for second-order elliptic problems [8], as well as iterative and multilevel methods for elliptic equations with coefficient jumps [9,10]. An extensive study on the parallel performance of algebraic multigrid solvers on Graphics Processing Units (GPUs) can be found in [11]. In the Domain Decomposition (DD) framework, numerous studies have addressed overlapping [12,13] and nonoverlapping [14–16] DD methods for DG discretizations of elliptic problems. However, these works did not consider the specific challenges of reaction–diffusion problems with discontinuous solutions which are the focus of this work, where the discrete solutions must preserve the discontinuities of the continuous problem. Among the few works addressing this issue, we mention the two-level algebraic multigrid method presented in [17], the analysis carried out in [18,19] and our previous work [20] on dual-primal preconditioners, in particular

* Corresponding author.
E-mail address: ngocmaimonica.huynh@unipv.it (N.M.M. Huynh).

https://doi.org/10.1016/j.cma.2024.117501
Received 29 May 2024; Received in revised form 30 September 2024; Accepted 20 October 2024
Available online 4 November 2024

the Balancing Domain Decomposition by Constraints (BDDC) preconditioner. While these BDDC preconditioners have been proven to be mathematically solid and to perform well on structured meshes or whenever the local connectivity graphs of the nodes are simple [20,21], their implementation is not straightforward. Indeed, high-performance libraries such as PETSc [22], typically require specific matrix and vector structures, which are not easily accessible to intermediate users. Moreover, the resulting reduced linear system is typically quite dense and can pose challenges when simulating examples with computational domains obtained through image segmentation, where the number of degrees of freedom is high and their distribution complex.

In order to overcome these issues, we consider here a DD method which presents the advantage of a simple nonoverlapping coarse problem combined with the power and simplicity of local solvers based on an overlapping partition of the domain. This method, known in the literature as generalized Dryja–Smith–Widlund (GDSW) preconditioner [23], has been largely studied for standard finite element discretizations of elliptic problems and a parallel implementation can be found in [24]. Several variants have been proposed by improving the construction of the coarse space [25,26] and by multilevel extensions [27].

In this paper, we extend the GDSW preconditioner to composite Discontinuous Galerkin discretizations of multicompartment reaction–diffusion problems. Since the abstract problem can be formulated as a collection of many subproblems that interact only on the interfaces of the related domain, there is a natural connection between the construction of the GDSW subspaces and the subproblems definition, as we will show in the next section. The main result of this paper is the proof of a scalable (i.e. independent of the number of subdomains N) and quasi-optimal (i.e. polylogarithmic in the ratio H/h between subdomain and element sizes) upper bound for the condition number of the GDSW preconditioned operator for composite DG discretizations of reaction–diffusion problems. The GDSW preconditioner is then applied to the recently proposed EMI (Extracellular - Membrane - Intracellular) reaction–diffusion system, modeling microscopically the spatio-temporal evolution of cardiac bioelectrical potentials.

The work is structured as follows: we start by presenting a generalized problem formulation in Section 2, along with a possible time discretization of its variational formulation. Section 3 introduces the standard GDSW preconditioner and the associated coarse and local spaces. In particular, we propose a suitable formulation of space subdivision. The main convergence result is proven in Section 4 and is confirmed numerically through extensive two-dimensional tests in Section 5. Several comments on further developments are given in the conclusive Section 6.

2. A multicompartment parabolic reaction–diffusion problem

The continuous model problem. Given $N+1$ generic domains $\Omega_i \subset \mathbb{R}^d$ with $i = 1, \dots, N+1$ and $d = 2, 3$, a time interval (0,T), such that the union of all the $\{\Omega_i\}_{i=1}^{N+1}$ domains forms a global domain Ω and such that $\Omega_i \cap \Omega_j = \emptyset$, with $i \neq j$, let us consider the following multicompartment parabolic reaction–diffusion problem: find $u = \{u_i\}_{i=1}^{N+1}$ such that it holds

$$\begin{cases} -\operatorname{div}(\sigma_i \nabla u_i) = 0 & \text{in } \Omega_i, \quad i = 1, \dots, N+1, \\ -n_i^T \sigma_i \nabla u_i = C_m \dfrac{\partial [\![u]\!]_{ij}}{\partial t} + F([\![u]\!]_{ij}) & \text{on } E_{ij} = \overline{\Omega}_i \cap \overline{\Omega}_j \subset \partial\Omega_i, \ i \neq j, \\ n^T \sigma_i \nabla u_i = 0 & \text{on } \partial\Omega_i \cap \partial\Omega, \\ u_i(0) = u_{i,0} & \text{in } \Omega_i, \quad i = 1, \dots, N+1. \end{cases} \tag{1}$$

Here, F is the reaction term and $[\![u]\!]_{ij} = u_i \cdot n_i - u_j \cdot n_j$ the jump between the value of u_i and its neighboring value u_j from the adjacent subdomain Ω_j along the common boundary E_{ij} (n_i is the outward normal to the ith subdomain), since u_i can be discontinuous across the domains. The constant C_m is the membrane capacitance for unit area of the membrane surface.

From an application viewpoint, this system could be seen as the union of (loosely) coupled problems: for instance, it can model the co-existence and interaction of different pollution agents in different regions over a time period; or it can represent the propagation of the electric potentials u_i at a cellular scale and the time evolution of the coupling of several cellular dynamics within any organ tissue (being this the brain, the cardiac muscle, etc.).

Remark 1. We consider $N+1$ domains (or problems) since in the numerical tests we will consider a particular application case where we will benefit from this notation. Moreover, since the purpose of this work is to study the convergence rate of a preconditioner for a composite Discontinuous Galerkin discretization of (1), we consider the simplified two-dimensional setting of our model problem ($d = 2$), leaving the three-dimensional case for further numerical studies.

The weak formulation for the coupled problem on Ω, by summing all the contributions from the $N+1$ domains, reads: given the initial data $u_{i,0} = u_i(0)$ for $i = 1, \dots N+1$, find $u = \{u_i\}_{i=1}^{N+1}$, $u_i \in L^2(0, T; H^1(\Omega_i))$, such that

$$\sum_{i=1}^{N+1} \int_{\Omega_i} \sigma_i \nabla u_i \nabla \phi_i \, dx + \frac{1}{2} \sum_{i=1}^{N+1} \sum_{E_{ij}} \int_{E_{ij}} \left(C_m \frac{\partial [\![u]\!]_{ij}}{\partial t} + F([\![u]\!]_{ij}) \right) [\![\phi]\!]_{ij} \, ds = 0, \tag{2}$$

for suitable test functions $\phi_i \in H^1(\Omega_i)$, $i = 1, \dots, N+1$.

Semidiscretization in time. In order to ease the subsequent analysis, we consider an implicit–explicit (IMEX) time discretization, where the diffusion term is treated implicitly and the reaction explicitly. Alternative implicit time discretizations could be considered as well, analogously to the Bidomain implicit discretizations studies in [28,29].

The time interval $(0, T)$ is subdivided into K intervals and, by defining the time step $\tau = t^{k+1} - t^k$, the following scheme arises: for $k = 1, \dots, K$, find $\{u_i^{k+1}\}_{i=1}^{N+1}$, with $u_i^{k+1} \in H^1(\Omega_i)$ such that $\forall \phi_i \in H^1(\Omega_i)$, $i = 1, \dots, N+1$

$$\frac{1}{2}\sum_{i=1}^{N+1}\sum_{E_{ij}}\int_{E_{ij}} C_m\frac{[\![u^{k+1}]\!]_{ij}-[\![u^{k}]\!]_{ij}}{\tau}[\![\phi]\!]_{ij}\,ds \quad + \sum_{i=1}^{N+1}\int_{\Omega_i}\sigma_i\nabla u_i^{k+1}\nabla\phi_i\,dx = -\frac{1}{2}\sum_{i=1}^{N+1}\sum_{E_{ij}}\int_{E_{ij}} F([\![u^{k}]\!]_{ij})[\![\phi]\!]_{ij}\,ds,$$

or, equivalently,

$$\frac{1}{2}\sum_{i=1}^{N+1}\sum_{E_{ij}}\int_{E_{ij}} C_m[\![u^{k+1}]\!]_{ij}[\![\phi]\!]_{ij}\,ds + \tau\sum_{i=1}^{N+1}\int_{\Omega_i}\sigma_i\nabla u_i^{k+1}\nabla\phi_i\,dx = \frac{1}{2}\sum_{i=1}^{N+1}\sum_{E_{ij}}\int_{E_{ij}} C_m[\![u^{k}]\!]_{ij}[\![\phi]\!]_{ij}\,ds - \tau\frac{1}{2}\sum_{i=1}^{N+1}\sum_{E_{ij}}\int_{E_{ij}} F([\![u^{k}]\!]_{ij})[\![\phi]\!]_{ij}\,ds.$$

Let the above quantities be recast as follows:

$$\begin{aligned} a_i(u,\phi) &:= \int_{\Omega_i}\sigma_i\nabla u_i\nabla\phi_i\,dx \\ p_i(u,\phi) &:= \frac{1}{2}\sum_{E_{ij}}\int_{E_{ij}}[\![u]\!]_{ij}[\![\phi]\!]_{ij}\,ds \\ f_i(\phi) &:= \frac{1}{2}\sum_{E_{ij}}\int_{E_{ij}}\left(C_m[\![u]\!]_{ij}[\![\phi]\!]_{ij} - \tau F([\![u]\!]_{ij})[\![\phi]\!]_{ij}\right)ds \end{aligned} \tag{3}$$

$$\widetilde{d}_i(u,\phi) := \tau a_i(u,\phi) + C_m p_i(u,\phi). \tag{4}$$

The semidiscrete problem at each time step can then be written in compact form as: find $u=\{u_i^{k+1}\}_{i=1}^{N+1}$, with $u_i^{k+1}\in H^1(\Omega_i)$ such that

$$d(u,\phi) := \sum_{i=1}^{N+1}\widetilde{d}_i(u,\phi) = f(\phi) := \sum_{i=1}^{N+1} f_i(\phi), \quad \forall\phi=\{\phi_i\}_{i=1}^{N+1}, \quad \phi_i\in H^1(\Omega_i). \tag{5}$$

The discrete problem. On each subdomain Ω_i, we consider a standard local finite element space $V^h(\Omega_i)$, and we denote by $V^h(\Omega)$ the product space of the $V^h(\Omega_i)$. The fully discrete problem at each time step is then given by: find $u=\{u_i\}_{i=1}^{N+1}\in V^h(\Omega)$ such that

$$d(u,\varphi) = f(\varphi), \qquad \forall\varphi=\{\varphi_i\}_{i=1}^{N+1}\in V^h(\Omega). \tag{6}$$

Denoting by $A_i\in\mathbb{R}^{N_{\text{dof}}\times N_{\text{dof}}}$ the local stiffness matrix associated with the bilinear form $a_i(\cdot,\cdot)$ and by $M_i\in\mathbb{R}^{N_{\text{dof}}\times N_{\text{dof}}}$ the local mass matrix associated with the bilinear form $p_i(\cdot,\cdot)$ (with N_{dof} the total number of degrees of freedom), then (6) can be written in matrix form as

$$\mathcal{K}\mathbf{u}=\mathbf{f}, \qquad \text{with} \qquad \mathcal{K}=\sum_{i=1}^{N+1}\mathcal{K}_i, \qquad \mathcal{K}_i=\tau A_i+M_i\in\mathbb{R}^{(N+1)\times(N+1)}. \tag{7}$$

The right-hand side of the above system is updated at each time step, and the resulting linear system is solved by the Preconditioned Conjugate Gradient (PCG) method. We will design and analyze an efficient and scalable preconditioner in the next section.

3. The GDSW preconditioner

In the following, we consider and study the theoretical convergence of an overlapping Schwarz preconditioner, known in the literature as the generalized Dryja–Smith–Widlund (GDSW) preconditioner, modified to comply with the structure of our multicompartment reaction–diffusion problem (1), where the solution on Ω is allowed to be discontinuous across the different subdomains Ω_i. The idea behind the GDSW algorithm is to combine a coarse space based on iterative substructuring techniques with local components based on classical overlapping Schwarz techniques [23].

We recall that the global domain Ω is the union of nonoverlapping (sub)domains Ω_i, $i=1,\dots,N+1$, and we have a finite element discretization on each subdomain; in the following we will denote with $\Gamma=\left(\cup_{i=1}^{N+1}\partial\Omega_i\right)\setminus\partial\Omega$ the interface between all subdomains. Our problem formulation allows also for non-matching discretizations across the subdomains (since the solution $u=\{u_i\}_{i=1}^{N+1}$ can be discontinuous), but for simplicity we analyze the case with matching nodes on the interface Γ between the subdomains. In a two-dimensional situation, this interface is composed of edges $\mathcal{E}^{ij}$ and vertices $\mathcal{V}^l$: the first are open subset of the interface Γ, containing all the degrees of freedom shared by two subdomains Ω_i and Ω_j, while the latter are endpoints of such edges. In three-dimensions, the interface would consist of faces (two-dimensional entities shared by two subdomains), edges (one-dimensional entities shared by more than two subdomains) and vertices (endpoints of edges).

Let us then construct an overlapping subdomain partition $\{\Omega_j'\}_j$ of Ω, for $j=1,\dots,N+1$, where each Ω_j is extended by a strip of depth $\delta>0$ (called overlap) of finite elements. Let us denote by $\Gamma_{j,\delta}$ this strip. Then $\Omega_j'=\Omega_j\cup\Gamma_{j,\delta}$. In the numerical tests in Section 5, we will consider only the case of minimal overlap, i.e. $\delta=h$ (see Fig. 1 on the left).

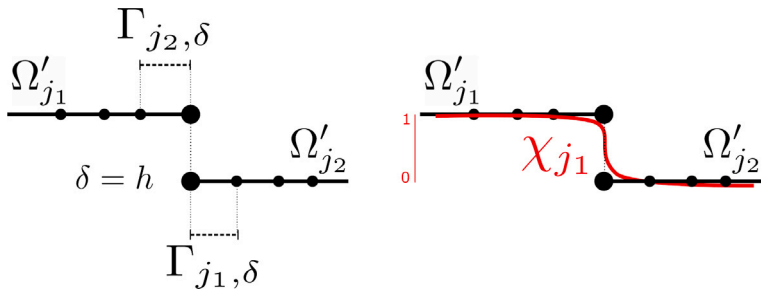

Fig. 1. Overlap between two overlapping subdomains Ω'_{j_1} and Ω'_{j_2} for the multicompartment problem described in system (1), 1-dimensional example. On the left, representation of the current minimal overlapping situation. On the right, the considered partition of unity basis function χ_{j_1} for subdomain Ω'_{j_1}.

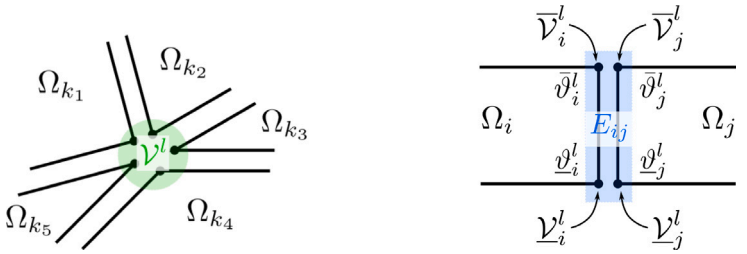

Fig. 2. Vertex and edge sharing, 2-dimensional example. On the left, the vertex $\mathcal{V}^l$ is shared by five nonoverlapping subdomains, therefore the set $\mathcal{V}_l^0$ contains five indices $\mathcal{V}_l^0 = \{k_1, k_2, k_3, k_4, k_5\}$. On the right, the vertices $\underline{\mathcal{V}}_i^l$, $\underline{\mathcal{V}}_j^l$ and $\overline{\mathcal{V}}_i^l$, $\overline{\mathcal{V}}_j^l$ represent the same geometric endpoints of the edge $E_{ij} \subset \partial\Omega_i$, but are referred to different subdomains.

3.1. GDSW coarse space

The coarse space V_0^C is chosen as the space spanned by the vertex and edges functions, described below, extended as discrete harmonic functions inside each subdomain Ω_i. These functions provide a partition of unity on the interface Γ. For each vertex $\mathcal{V}^l$ we have as many vertex functions as the number of subdomains that share that vertex. Denote by $\mathcal{V}_l^0$ the set of indices k of subdomain Ω_k that share vertex $\mathcal{V}^l$, for all $l = 1, \dots, N_{\text{vertices}}$, where N_{vertices} is the total number of vertices (see Fig. 2, left). Then the vertex functions associated with vertex $\mathcal{V}^l$ are given by

$$\vartheta^l(x) = \{\vartheta_k^l(x)\}_{k \in \mathcal{V}_l^0},$$

where ϑ_k^l is the coarse function associated to $\mathcal{V}^l$ that has support in Ω_k. The edge functions $\vartheta_{E_{ij}}(x)$ (represented in Fig. 2, right) are instead unique for each edge E_{ij}, and are equal 1 on edge E_{ij} and extended harmonically elsewhere.

Thus, the coarse component $u_0 \in V_0^C$ can be written as

$$u_0 = \sum_{\mathcal{V}^l} \sum_{k \in \mathcal{V}_l^0} u_k(\mathcal{V}^l)\, \vartheta_k^l(x) + \sum_{E_{ij}} \bar{u}_{E_{ij}}\, \vartheta_{E_{ij}}(x), \tag{8}$$

where $\bar{u}_{E_{ij}}$ is the average of u over the edge E_{ij}. The projection P_0 onto the coarse space V_0^C is defined as

$$d(P_0 u, v) = d(u, v), \qquad \forall v \in V_0^C.$$

3.2. GDSW local spaces

We recall that the local nonoverlapping finite element spaces have been denoted by $V_i = V^h(\Omega_i)$, while the product space can be written as $V = V_1 \times \cdots \times V_{N+1}$. We then define the local space

$$V_i' = \{v \in V \,:\, v = 0 \quad \text{in } \Omega \backslash \Omega_i'\}.$$

This space can also be written as

$$V_i' = V_i \times \{\phi_j \,:\, \phi_j \neq 0 \text{ on } \partial\Omega_i,\ \phi_j \notin V_i\}.$$

Since $V_i' \subset V$, any function $u_i' \in V_i'$ can be written as $u_i' = \{u_{i,j}'\}_{j=1}^{N+1}$, where $u_{i,j}'$ denotes the projection of function u_i' on the subdomain Ω_j'. Let χ_i, $i = 1, \dots, N+1$ be a partition of unity as defined in [23]. We recall that these functions vary between 0 and 1, their gradients are bounded by C/δ_j and vanish outside the overlap $\Gamma_{j,\delta}$. Any function $u \in V$ can be written as

$$u = u_0 + \sum_{i=1}^{N+1} u_i', \qquad u_0 \in V_0^C, \quad u_i' \in V_i', \text{ for } i = 1, \dots, N+1.$$

where $u_0 \in V_0^C$ has been defined in (8) and $u_i' \in V_i'$ are given by $u_i' = I^h(\chi_i(u - u_0)) \in V_i' \subset V$, where I^h interpolates into the product space $V^h(\Omega)$. The projection-like operators P_i onto the local space V_i' are defined as $P_i = I_i \tilde{P}_i$ (with I_i being the local interpolant), where

$$d(P_i u, v_i) = d(u, v_i), \qquad \forall v_i \in V_i'.$$

Our GDSW preconditioned operator is then defined as

$$P_{ad} = P_0 + \sum_{i=1}^{N+1} P_i. \tag{9}$$

Remark 2 (*Technical Assumptions*)**.** We will consider domains with the same geometrical properties as in Ref. [23] (namely, Ω_i are John domains, each with a shape-regular triangulation), in order to consider the same technical results stated in that work. The numerical tests presented in Section 5 consider simpler and more trivial domains, and in that case some of the assumptions can be dropped and the convergence result may be sharpened. Nevertheless, to enhance readability, we will not include here these technical tools, but we will refer to the specific Lemmas whenever required.

We prove here an auxiliary result that will be used in the proof of the convergence rate bound; this is an adaptation of the bound (4.3) from [23].

Lemma 1. *Let u_0 be the GDSW coarse function defined in (8). Then, for the multicompartment problem defined in (6), it holds*

$$\|u - u_0\|^2_{L^2(\Omega_i)} \leq C \left(1 + \log \frac{H}{h}\right)^2 H^2 |u|^2_{H^1(\Omega_i)},$$

with H and h the maximum subdomain and finite element diameters, respectively.

Proof. By adding and subtracting $\bar{u}_{\Omega_i}$, the average of u on the subdomain Ω_i, it remains to bound only $\|u_0 - \bar{u}_{\Omega_i}\|_{L^2(\Omega_i)}$, since $\|u - \bar{u}_{\Omega_i}\|_{L^2(\Omega_i)}$ can be bounded with the energy norm of u by a Poincaré inequality type. The first term can be written as the sum of three parts, each with support in Ω_i,

$$u_0 - \bar{u}_{\Omega_i} = \sum_{\mathcal{V}^l} \left(u_i(\mathcal{V}^l) - \bar{u}_{\Omega_i}\right) \vartheta_i^l(x) \tag{10}$$

$$+ \sum_{\mathcal{V}^l} \sum_{\substack{k \in \mathcal{V}_l^0 \\ k \neq i}} \left(u_k(\mathcal{V}^l) - \bar{u}_{\Omega_i}\right) \vartheta_k^l(x) \tag{11}$$

$$+ \sum_{E_{ij}} \left(\bar{u}_{E_{ij}} - \bar{u}_{\Omega_i}\right) \vartheta_{E_{ij}}(x), \tag{12}$$

containing contributions from the vertices of Ω_i themselves (line Eq. (10)), the adjacent vertices to each vertex of Ω_i (line Eq. (11)) and the edges of Ω_i (line Eq. (12)) respectively. The term (10) can be bounded by using [23, Lemma 3.2] as follows:

$$\begin{aligned} \| \sum_{\mathcal{V}^l} \left(u_i(\mathcal{V}^l) - \bar{u}_{\Omega_i}\right) \vartheta_i^l(x) \|^2_{L^2(\Omega_i)} &\leq C \sum_{\mathcal{V}^l} \int_{\Omega_i} |u_i(\mathcal{V}^l) - \bar{u}_{\Omega_i}|^2 |\vartheta_i^l(x)|^2 \, d\Omega \\ &\leq C \left(1 + \log \frac{H}{h}\right)^2 |u|^2_{H^1(\Omega_i)} \sum_{\mathcal{V}^l} \int_{\Omega_i} |\vartheta_i^l(x)|^2 \, d\Omega \quad \leq C \left(1 + \log \frac{H}{h}\right)^2 H^2 |u|^2_{H^1(\Omega_i)}. \end{aligned}$$

The remaining terms (11) and (12) can be treated analogously. □

4. Theoretical convergence rate bounds

We are now ready to prove the convergence of GDSW preconditioners for the considered composite discontinuous Galerkin discretization of problem (1).

Theorem 1. *The condition number of the GDSW preconditioned operator P_{ad} defined in (9) for the discrete problem (6), when considering a coarse space with vertex and edge basis functions, as described in Section 3, satisfies the bound*

$$cond\,(P_{ad}) \leq C \Phi_{\tau,\sigma_M,\sigma_m} \left(1 + \frac{H}{\delta}\right) \left(1 + \log \frac{H}{h}\right)^2,$$

where Φ depends on the conductivity coefficients, the time-step size τ, the subdomain diameter H and finite element size h

$$\Phi_{\tau,\sigma_M,\sigma_m} = \left(\sigma_M + \frac{C_m}{\tau\sigma_m}\right) \qquad \sigma_m = \min_i |\sigma_i|, \quad \sigma_M = \max_i |\sigma_i|, \tag{13}$$

and C is a positive constant independent of N, h, H, τ.

Remark 3. The dependence of $\Phi_{\tau,\sigma_M,\sigma_m}$ on the time-step size τ, σ_M and σ_m is not observed in the results of the numerical tests in Section 5, indicating that the theoretical bound might not be sharp in τ, σ_M and σ_m. We remark that, by assuming continuity across the interface, the same result obtained in [23] would hold.

Proof. The proof is based on general abstract Schwarz theory as well as previous works on GDSW preconditioners, see [23,25,26,30]. In particular, we are required to verify three assumptions known as strengthened Cauchy–Schwarz inequality, local stability and stable decomposition, see [30]. However, by considering a standard coloring argument, the strengthened Cauchy–Schwarz inequality can be satisfied with a constant upper bound. Moreover, the local stability assumption holds true, since we use exact local solvers. Therefore, we will only need to prove a stable decomposition for the considered subspace decomposition.

We proceed as in standard Schwarz theory by estimating the constant C_0^2 required by the stable decomposition [30] and by considering the coarse and local solvers separately.

Coarse solver. As usually done in domain decomposition algorithms, we work with one subdomain Ω_i per time. We consider $u - \bar{u}_{\Omega_i}$, and instead of (8) we consider $u_0 - \bar{u}_{\Omega_i}$, being $\bar{u}_{\Omega_i}$ the average of u over subdomain Ω_i:

$$\bar{u}_{\Omega_i}(x) = \bar{u}_{\Omega_i}\left(\sum_{\mathcal{V}^l}\sum_{k\in\mathcal{V}_l^0} \vartheta_k^l(x) + \sum_{E_{ij}} \vartheta_{E_{ij}}(x)\right).$$

Thus we want to bound the energy

$$\widetilde{d}_i(u_0 - \bar{u}_{\Omega_i}, u_0 - \bar{u}_{\Omega_i}) = \tau\, a_i(u_0 - \bar{u}_{\Omega_i}, u_0 - \bar{u}_{\Omega_i}) + p_i(u_0 - \bar{u}_{\Omega_i}, u_0 - \bar{u}_{\Omega_i}).$$

The first term can be treated in the following way: recalling the coarse decomposition (8), let us write explicitly $u_0 - \bar{u}_{\Omega_i}$:

$$u_0 - \bar{u}_{\Omega_i} = \sum_{\mathcal{V}^l}\left(u_i(\mathcal{V}^l) - \bar{u}_{\Omega_i}\right)\vartheta_i^l(x) + \sum_{\mathcal{V}^l}\sum_{\substack{k\in\mathcal{V}_l^0\\ k\neq i}}\left(u_k(\mathcal{V}^l) - \bar{u}_{\Omega_i}\right)\vartheta_k^l(x) + \sum_{E_{ij}}\left(\bar{u}_{E_{ij}} - \bar{u}_{\Omega_i}\right)\vartheta_{E_{ij}}(x).$$

The energy norm induced by the bilinear form $a_i(\cdot,\cdot)$ can be estimated by

$$\begin{aligned}
a_i(u_0 - \bar{u}_{\Omega_i}, u_0 - \bar{u}_{\Omega_i}) &= \int_{\Omega_i} \sigma_i\, \nabla(u_0 - \bar{u}_{\Omega_i})\cdot\nabla(u_0 - \bar{u}_{\Omega_i}) \\
&\leq C\sum_{\mathcal{V}^l}\int_{\Omega_i}\sigma_i\left(u_i(\mathcal{V}^l) - \bar{u}_{\Omega_i}\right)^2 |\nabla\vartheta_i^l(x)|^2 + \sum_{\mathcal{V}^l}\sum_{\substack{k\in\mathcal{V}_l^0\\ k\neq i}}\int_{\Omega_i}\sigma_i\left(u_k(\mathcal{V}^l) - \bar{u}_{\Omega_i}\right)^2 |\nabla\vartheta_k^l(x)|^2 + \sum_{E_{ij}}\int_{\Omega_i}\sigma_i\left(\bar{u}_{E_{ij}} - \bar{u}_{\Omega_i}\right)^2 |\nabla\vartheta_{E_{ij}}(x)|^2 \\
&\overset{(A)}{\lesssim} |\sigma_i|\left(1 + \log\frac{H}{h}\right)|u|^2_{H^1(\Omega_i)}\left(\sum_{\mathcal{V}^l}|\vartheta_i^l|^2_{H^1(\Omega_i)} + \sum_{\mathcal{V}^l}\sum_{\substack{k\in\mathcal{V}_l^0\\ k\neq i}}|\nabla\vartheta_k^l(x)|^2 + \sum_{E_{ij}}|\vartheta_{E_{ij}}|^2_{H^1(\Omega_i)}\right) \\
&\overset{(B)}{\lesssim} |\sigma_i|\left(1 + \log\frac{H}{h}\right)^2 |u|^2_{H^1(\Omega_i)} \leq \left(1 + \log\frac{H}{h}\right)^2 a_i(u,u)
\end{aligned} \tag{14}$$

For inequality (A), the terms $u_k(\mathcal{V}^l) - \bar{u}_{\Omega_i}$ and $\bar{u}_{E_{ij}} - \bar{u}_{\Omega_i}$ can be bounded using [23, Lemma 3.2], while (B) is obtained thanks to the fact that the first seminorm in the brackets is bounded and the second is zero by definition, while the last term can be bounded considering [23, Lemma 3.4].

Regarding the jump term $p_i(\cdot,\cdot)$, it is useful to write explicitly the average $\bar{u}_{\Omega_i}$ over the edge E_{ij} in terms of edge basis functions (see Fig. 2 for the notation):

$$\bar{u}_{\Omega_i}(x) = \begin{cases} \bar{u}_{\Omega_i}\left(\bar{\vartheta}_i^l(x) + \vartheta_{E_{ij}}(x) + \underline{\vartheta}_i^l(x)\right) \\ \bar{u}_{\Omega_i}\left(\bar{\vartheta}_j^l(x) + \vartheta_{E_{ij}}(x) + \underline{\vartheta}_j^l(x)\right) \end{cases}$$

We need to focus on the jump

$$[\![u_0 - \bar{u}_{\Omega_i}]\!]_{ij} = \left(u_{0,i} - \bar{u}_{\Omega_i}\right) - \left(u_{0,j} - \bar{u}_{\Omega_i}\right),$$

being

$$u_{0,i} = u(\overline{\mathcal{V}}_i^l)\,\bar{\vartheta}_i^l(x) + u(\underline{\mathcal{V}}_i^l)\,\underline{\vartheta}_i^l(x) + \bar{u}_{E_{ij}}\vartheta_{E_{ij}}(x), \qquad u_{0,j} = u(\overline{\mathcal{V}}_j^l)\,\bar{\vartheta}_j^l(x) + u(\underline{\mathcal{V}}_j^l)\,\underline{\vartheta}_j^l(x) + \bar{u}_{E_{ij}}\vartheta_{E_{ij}}(x)$$

The inner edge contribution $\bar{u}_{E_{ij}}\vartheta_{E_{ij}}(x)$ can be neglected, since it appears from both sides of E_{ij}. Thus, if we focus on only one endpoint of E_{ij} (for instance $\overline{\mathcal{V}}^l$), we need to estimate the jump of $\bar{w} = (u(\bar{\vartheta}_i^l) - \bar{u}_{\Omega_i})\,\bar{\vartheta}_i^l(x) - (u(\bar{\vartheta}_j^l) - \bar{u}_{\Omega_i})\,\bar{\vartheta}_j^l(x)$:

$$p_i(\bar{w},\bar{w}) \lesssim C_m \sum_{E_{ij}} \left(1+\log\frac{H}{h}\right)|u|^2_{H^1(\Omega_i)} \left(\|\bar{\vartheta}_i^l(x)\|^2_{L^2(E_{ij})} + \|\bar{\vartheta}_j^l(x)\|^2_{L^2(E_{ij})}\right) \lesssim C_m \left(1+\log\frac{H}{h}\right)|u|^2_{H^1(\Omega_i)} \lesssim \frac{C_m}{|\sigma_i|}\left(1+\log\frac{H}{h}\right) a_i(u,u) \tag{15}$$

In the same fashion, it is possible to estimate the jump for the term $\underline{w} = (u(\underline{\vartheta}_i^l) - \bar{u}_{\Omega_i})\,\underline{\vartheta}_i^l(x) - (u(\underline{\vartheta}_j^l) - \bar{u}_{\Omega_i})\,\underline{\vartheta}_j^l(x)$. By definition,

$$\widetilde{d}_i(u_0 - \bar{u}_{\Omega_i}, u_0 - \bar{u}_{\Omega_i}) = \tau\, a_i(u_0 - \bar{u}_{\Omega_i}, u_0 - \bar{u}_{\Omega_i}) + p_i(u_0 - \bar{u}_{\Omega_i}, u_0 - \bar{u}_{\Omega_i}).$$

We can estimate the energy of the first term with the bound obtained in (14) while the second term can be bounded by (15). Therefore,

$$\widetilde{d}_i(u_0 - \bar{u}_{\Omega_i}, u_0 - \bar{u}_{\Omega_i}) \le C\left(1+\frac{C_m}{\tau|\sigma_i|}\right)\left(1+\log\frac{H}{h}\right)^2 \widetilde{d}_i(u,u),$$

thus leading to

$$d(u_0 - \bar{u}_{\Omega_i}, u_0 - \bar{u}_{\Omega_i}) \le C\left(1+\frac{C_m}{\tau\sigma_m}\right)\left(1+\log\frac{H}{h}\right)^2 d(u,u), \qquad \text{where} \quad \sigma_m = \min_{i=1,\dots,N+1}|\sigma_i|.$$

Local solvers. In Section 3.2 we have defined $u = u_0 + \sum_{i=1}^{N+1} u_i'$ for $u_0 \in V_0^C$ and $u_i' = I^h(\chi_i(u-u_0)) =: I^h\chi_i w \in V_i'$, with $i = 1,\dots,N+1$. We recall that, for all $u_i', v_i' \in V_i'$, $u_i' = \{u_{i,j}'\}_{j=0}^N$,

$$\begin{aligned} d_i(u_i',v_i') &:= d(u_i',v_i') = \tau\sum_{k=1}^{N+1}\sigma_k\int_{\Omega_k}\nabla u_{i,k}'\,\nabla v_{i,k}' + \sum_{E_{kj}} C_m\int_{E_{kj}}(u_{i,k}'-u_{i,j}')(v_{i,k}'-v_{i,j}') \\ &= \tau\sigma_i\int_{\Omega_i}\nabla u_{i,i}'\,\nabla v_{i,i}' + \tau\sum_{j\,:\,\Omega_j\cap\Gamma_{i,\delta}\neq\emptyset}\sigma_j\int_{\Omega_j\cap\Gamma_{i,\delta}}\nabla u_{i,j}'\,\nabla v_{i,j}' \qquad (16) \\ &+ \sum_{j\,:\,\partial\Omega_i\cap\partial\Omega_j\neq\emptyset} C_m\int_{E_{ij}}(u_{i,i}'-u_{i,j}')(v_{i,i}'-v_{i,j}'). \qquad (17) \end{aligned}$$

Here the same considerations made in the proof of [23, Theorem 3.1] hold. Thus, the energy norms in line (16) (consider for instance the first term — the second follows analogously) can be bounded as in the proof of [30, Lemma 3.10]:

$$|u_{i,i}'|^2_{H^1(\Omega_i)} \le |I^h(\chi_i w)|^2_{H^1(\Omega_i)} \le C\left[\left(1+\frac{H}{\delta}\right)|w|^2_{H^1(\Omega_i)} + \frac{1}{H\delta}\,\|\,w\,\|^2_{L^2(\Omega_i)}\right],$$

where δ is the common overlap parameter. Each of the above contributions can be bounded as follows.

(i) By considering the triangle inequality and the result obtained in the coarse solver for the energy norm, it holds

$$|w|^2_{H^1(\Omega_i)} \lesssim \left(1+\log\frac{H}{h}\right)^2 |u|^2_{H^1(\Omega_i)}.$$

(ii) Thanks to Lemma 1, we have

$$\|\,w\,\|^2_{L^2(\Omega_i)} \le C\left(1+\log\frac{H}{h}\right)^2 H^2|u|^2_{H^1(\Omega_i)}.$$

Collecting the above contributions leads to the following bound for the energy norms of line (16):

$$|\sigma_i||u_{i,i}'|^2_{H^1(\Omega_i)} \le C|\sigma_i|\left(1+\log\frac{H}{h}\right)^2\left[\left(1+\frac{H}{\delta}\right)|u|^2_{H^1(\Omega_i)} + \frac{H}{\delta}|u|^2_{H^1(\Omega_i)}\right] \le C|\sigma_i|\left(1+\log\frac{H}{h}\right)^2\left(1+\frac{H}{\delta}\right)|u|^2_{H^1(\Omega_i)}.$$

Regarding the jump contributions in line (17), it holds

$$p_i(u_i',u_i') = p_i(I^h\chi_i w, I^h\chi_i w) \lesssim p_i(u,u) + p_i(u_0,u_0).$$

The first term appears in the bilinear form $d_i(\cdot,\cdot)$, while the bound for the second term follows the same proof procedure as in the coarse solver by adding and subtracting the average $\bar{u}_{\Omega_i}$, see Eq. (15). Therefore, the local solvers satisfy the bound

$$d_i(u_i',u_i') = d_i(I^h\chi_i w, I^h\chi_i w) \le C\left[\sigma_M\left(1+\frac{H}{\delta}\right) + \frac{C_m}{\tau\sigma_m}\right]\left(1+\log\frac{H}{h}\right)^2 d_i(u,u),$$

where $\sigma_M = \max_{i=1,\dots,N+1}|\sigma_i|$ and $\sigma_m = \max_{i=1,\dots,N+1}|\sigma_i|$.

In conclusion, by collecting the above result and the coarse solver estimate,

$$d(u_0,u_0) + \sum_{i=1}^{N+1} d_i(u_i',u_i') \le C\left(\sigma_M + \frac{C_m}{\tau\sigma_m}\right)\left(1+\frac{H}{\delta}\right)\left(1+\log\frac{H}{h}\right)^2 d(u,u). \quad \square$$

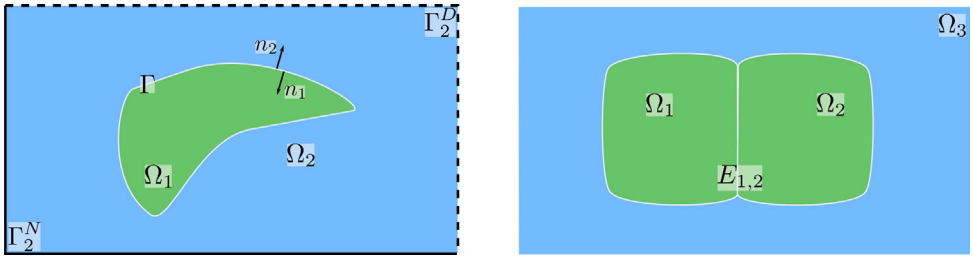

Fig. 3. Left: representation of the situation described in system (1), with only one cell Ω_1 (green) immersed in the extracellular liquid (light blue); the external boundary of the extracellular space Ω_2 is divided into Γ_2^D (black, dashed) and Γ_2^N (black, solid), with boundary conditions given in (19). Right: representation of the situation described in system (1) considering two neighboring cells Ω_1 and Ω_2, with common boundary $E_{1,2}$. (For interpretation of the references to color in this figure legend, the reader is referred to the web version of this article.)

Remark 4. In Section 5, the numerical tests consider a minimal overlap, thus $\delta = h$, due to the considered model example. Therefore, the expected theoretical convergence estimate is given by

$$\text{cond}\,(P_{ad}) \leq C\,\Phi_{\tau,\sigma_M,\sigma_m}\left(1+\frac{H}{h}\right)\left(1+\log\frac{H}{h}\right)^2,$$

with Φ defined in (13).

5. An application to the cardiac EMI model

We now consider a particular application from the field of electrophysiology to numerically tests the proposed preconditioner. Our focus is the so-called cardiac EMI model[1] [3–5,31], which provides a microscopic representation of the electrical propagation in the cardiac tissue by means of diffusion equations for each single cell coupled through a (possibly nonlinear) reaction term on the boundaries (cell membranes). This innovative model overcomes the well-established cardiac Bidomain model [32], since it represents the extracellular space as well as the intracellular space and the cell membrane as individuals, allowing for realistic characterization of each. While for the Bidomain equations we can find several works related to its mathematical properties [32–35] and solution strategies [28,29,36–42], these various aspects for the cardiac EMI model are still open problems.

5.1. The EMI microscopic description of cardiac electrical propagation

We consider N connected cells immersed in the extracellular liquid, which altogether form the cardiac tissue Ω, where generally $\Omega \subset \mathbb{R}^d$, with $d \in \{2,3\}$; in the following numerical experiments we will consider $d = 2$, in compliance with the proposed convergence analysis. It is straightforward to visualize the parallelism between these $N+1$ objects and the nonoverlapping partition $\{\Omega_i\}_i$, with $i = 1,\dots,N+1$ (by denoting with Ω_{N+1} the extracellular subdomain). The interaction between each cell, the extracellular media and their neighbors happens by means of ionic exchanges, which provide the reaction term on the boundaries $\partial\Omega_i$. These currents are allowed to propagate among the intracellular spaces through the gap junctions, special protein channels which allow the passage of ions directly between two intracellular environments, [43].

The situation depicted on the left of Fig. 3 can be modeled by system (1), where we need to add the ionic equations

$$\frac{\partial c}{\partial t} - C(\llbracket u\rrbracket_{ij}, w, c) = 0, \qquad \frac{\partial w}{\partial t} - R(\llbracket u\rrbracket_{ij}, w) = 0, \tag{18}$$

that model the ion flow dynamic by means of ordinary differential equations, describing the time evolution of ion concentrations c and gating variables w by means of given functions C and R respectively. Here, the transmembrane voltage $\llbracket u\rrbracket_{ij} = u_i - u_j$ represents the jump in the values of the electric potentials between two neighboring cells i and j. Thus, the reaction term $F(\cdot)$ will depend also on the gating and concentration variables, representing either the ionic current $I_{\text{ion}}(\llbracket u\rrbracket_{ij}, c, w)$ or the gap junctions $G(\llbracket u\rrbracket_{ij})$ (which we assume here to be linear in the potential jump). We assume that the (extracellular) potential is fixed on part of the external boundary Γ_{N+1}^D while the remaining $\Gamma_{N+1}^N = \Gamma \backslash \Gamma_{N+1}^D$ is insulated:

$$u_{N+1} = 0 \quad \text{on } \Gamma_{N+1}^D, \qquad -n_{N+1}^T \cdot \sigma_{N+1}\,\nabla u_{N+1} = 0 \quad \text{on } \Gamma_{N+1}^N. \tag{19}$$

[1] The acronym EMI stands for Extracellular, cell Membrane and Intracellular spaces, since this formulation takes into account each of these three separate fields.

In this framework, σ_i is the conductivity coefficient[2] in Ω_i and n_i^T the outward normal on $\partial\Omega_i$. We refer to [4,31] for a formal derivation of the complete EMI system.

The solution obtained from such problem is defined up to an arbitrary constant: in order to ensure uniqueness from a numerical point of view, we impose zero average for the extracellular component u_{N+1} over the domain.

In conclusion, the cardiac EMI model reads

$$\begin{cases} -\operatorname{div}(\sigma_i \nabla u_i) = 0 & \text{in } \Omega_i \quad \forall i = 1, \dots, N+1, \\ u_i - u_j = [\![u]\!]_{ij} & \text{on } E_{ij}, \\ -n_i^T \sigma_i \nabla u_i = C_m \dfrac{\partial [\![u]\!]_{ij}}{\partial t} + F([\![u]\!]_{ij}, c, w) & \text{on } E_{ij}, \\ \dfrac{\partial c}{\partial t} - C([\![u]\!]_{ij}, w, c) = 0, \qquad \dfrac{\partial w}{\partial t} - R([\![u]\!]_{ij}, w) = 0 & \text{on } E_{ij}, \\ u_i(0) = u_{i,0}, \qquad w(0) = w_0, \qquad c(0) = c_0, & \text{in } \Omega_i \quad \forall i = 1, \dots, N+1. \end{cases} \tag{20}$$

We consider a splitting strategy for the time solution of system (20). At each time step, we solve first the ionic model, given the jump $[\![u]\!]_{ij}$ from the previous time step; then, we update the cell-by-cell model with the newly computed c and w, and solve it with respect to the electric potential. With this approach, we can easily refer to the discretized formulation derived in Section 2 and the preconditioning technique introduced in Sec. 3, obtaining an EMI-GDSW preconditioner. Another recently proposed approach considers a boundary integral formulation of system (20), see [44].

5.2. Numerical tests

We consider a Matlab implementation of our EMI-GDSW preconditioner for a two-dimensional rectangular geometry where the extracellular domain frames a group of cells. Each cell (subdomain) presents an aspect ratio of 6:1 finite elements, in order to correctly represent the average aspect ratio of an actual cardiac myocyte. Our code considers a linear gap junction between cells, each coinciding with an edge E_{ij}, and the Aliev–Panfilov ionic model [45] for the update of the gating variables; this model does not include concentration variables. We fix the time-step size to $\tau = 0.05$ ms, except for Section 5.2.3, where the parameter τ is varied between 0.005 and 0.1 ms in order to study its effects on the EMI-GDSW convergence rate. The external current needed for the activation is applied at the bottom-left corner of the domain for 1 ms, with an intensity of 50 mA/cm^2; the total simulation time is of $[0, 5]$ ms. The initial value for the potential $u_i(0)$ is set to -85 mV, while the initial gating w_0 value is set to 0. Unless otherwise specified, the conductivity coefficients are $\sigma_i = 3 \times 10^{-3}$ in all cells.

The discrete linear system (7) arising at each time step is solved through an iterative Conjugate Gradient method, either unpreconditioned (CG) or with preconditioning. The stopping criterion compares the L^2-norm of the relative (preconditioned) residual with a fixed tolerance of 10^{-6}. We implemented a GDSW preconditioner with a coarse problem spanned by the subdomain vertex and edge basis functions, see Sec. 3.1 for further details. For comparison, we also consider the classical one-level Additive Schwarz algorithm (AS) without coarse space; see [30, Chapters 1-3] for further details. Both algorithms consider a minimal overlap of $\delta = h$, in order to exploit the overlap between cells that follows from the EMI formulation.

All the tests have been performed on a Linux workstation equipped with an Intel i9-10980XE CPU with 18 cores running at 3.00 GHz.

5.2.1. Scalability tests

We start with numerical results investigating the scalability of the proposed EMI-GDSW preconditioned solver. We consider a time interval of $[0, 5]$ ms, for a total of 100 uniform time steps. The number of cells (subdomains) considered varies from $N = 2 \times 2$ to $N = 32 \times 32$, each one discretized by 24×4 finite elements. We report the condition number (k_2) and the number of linear iterations (it) at the final time step of the simulation; see Fig. 4(a) and Fig. 4(b). Fig. 4(a) reports also dimensions and number of nonzero (nnz) entries of the EMI-GDSW coarse solver matrix, while Fig. 5 (top row) shows its sparsity pattern. If compared to the EMI-BDDC coarse solver matrices (Fig. 5, bottom row) proposed in [20], given the same number of cells, we note that, in addition to the obvious difference of the two coarse space sizes, the number of nonzero entries for the EMI-GDSW coarse matrices is more than three times higher, and the sparsity pattern is less compact. The results show that the GDSW preconditioner has a scalable performance in all the cases considered, in terms of both number of linear iterations and condition numbers. Both these parameters mildly increase while initially increasing the number of cells N, but they approach a constant upper bound afterwards, in agreement with the main bound of Theorem 1, since the ratio H/h is kept constant in these tests. On the other hand, for both unpreconditioned CG as well as AS, the iteration counts and condition numbers increase with increasing N.

[2] In general σ_i are tensors; however, in this work, we have treated them as scalar since the EMI model assumes isotropic diffusion in the cells and in the extracellular matrix. This is motivated by the fact that the pronounced anisotropy in the homogenized bidomain model is an effect of the cellular geometry, which here in the EMI model is resolved explicitly.

nb cells	N_{dof}	EMI-GDSW k_2	it	dim_{coarse} (%)	AS k_2	it	CG k_2	it
2×2	1140	64.1	32	28 (2.46%)	149.2	30	2.20e+03	124
4×4	3200	90.1	43	112 (3.50%)	632.4	58	7.09e+03	204
8×8	10320	104.0	51	424 (4.11%)	2.61e+03	106	2.50e+04	355
12×12	21440	112.2	54	928 (4.33%)	5.87e+03	157	5.26e+04	494
16×16	36560	116.2	55	1624 (4.44%)	1.03e+04	205	8.94e+04	624
20×20	55680	119.8	57	2512 (4.51%)	1.58e+04	252	1.32e+05	756
24×24	78800	120.7	57	3592 (4.56%)	2.20e+04	297	1.79e+05	877
28×28	105920	121.9	58	4864 (4.59%)	2.73e+04	332	1.90e+05	921
32×32	137040	122.9	59	6328 (4.62%)	3.35e+04	368	1.78e+05	932

(a) Condition number (k_2) and linear iterations (it) at final time $t = 5$ ms for EMI-GDSW (left), AS (center), unpreconditioned CG (right). Dimension and percentage w.r.t. N_{dof} for the EMI-GDSW coarse solver is also reported.

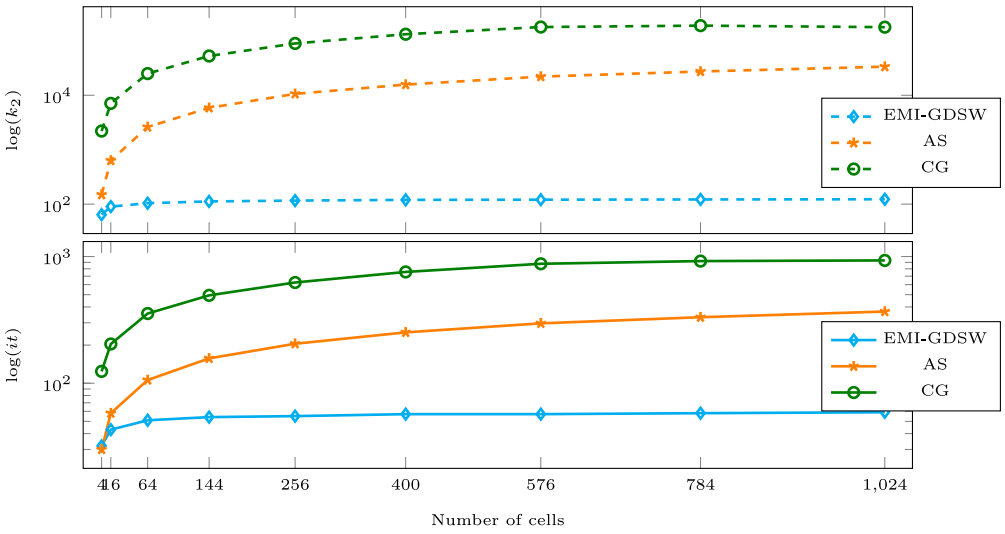

(b) Plots of condition numbers (k_2) and linear iterations (it) from Table a) above.

Fig. 4. *EMI-GDSW Scalability tests* on $[0, 5]$ ms. Condition number (k_2) and linear iterations (it) at final time $t = 5$ ms. Fixed time step $\tau = 0.05$. Increasing number of cells from 4 to 1024, each discretized with 24×4 finite elements.

5.2.2. Optimality tests

We then test the quasi-optimality of our method by fixing the number of cells (subdomains) to be $N = 4 \times 4$) and decrease the mesh size h, i.e. increase the ratio H/h. In these tests, the EMI-GDSW coarse solver has dimensions 112×112 and 1844 nonzero entries. Fig. 6(a) and Fig. 6(b) show again that EMI-GDSW has a much better performance of both AS and unpreconditioned CG. The polylogarithmic growth of the EMI-GDSW condition number is not easily detectable for this range of H/h, but the growth seems definitely less than linear, as shown in Fig. 6(b). In order to detect the asymptotic behavior of the EMI-GDSW condition number, higher values of H/h should be explored as in [46], but this was currently beyond our actual computational capability using a Matlab implementation on a workstation.

5.2.3. Dependence on the time-step size

Here we study the convergence rate dependence of the proposed solver on the time-step size τ. We consider $N = 12 \times 12$ cells, each one discretized with 24×4 Q1 finite elements. The time interval is $[0, 5]$ ms, where we vary τ from 0.005 to 0.1 ms. As in our previous study [20], we observe that the condition number (k_2) and the iteration counts (it) for both unpreconditioned CG and AS solvers increase when the time-step size τ is decreased, see Fig. 7(a) and Fig. 7(b). On the other hand, the EMI-GDSW preconditioner is only marginally affected by the reduction of τ, yielding almost bounded k_2 and it values. We remark that the unpreconditioned discrete problem already shows an increasing condition number and iteration counts for decreasing values of τ, see Fig. 7(b), even if we would expect the problem to be mass dominated. One reason for this could be that the mass matrix of the EMI problem is associated only to the potential jumps on subdomains/cells interfaces, which is different from the standard case.

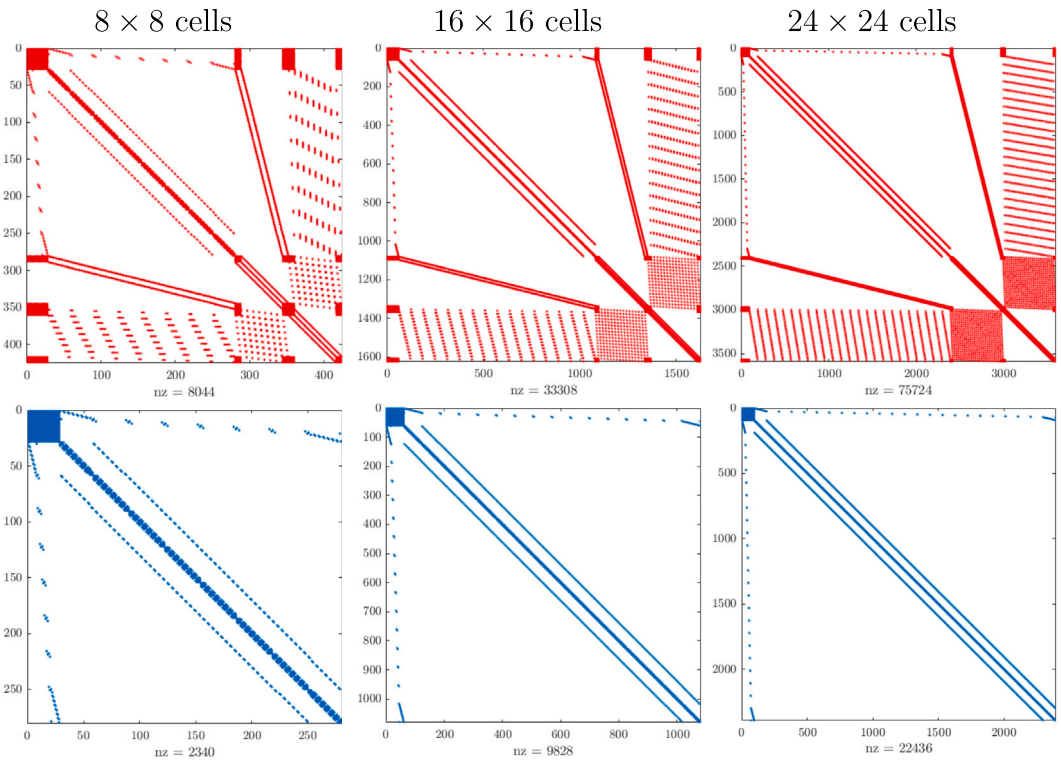

Fig. 5. Sparsity pattern of EMI-GDSW (top row, red) and EMI-BDDC (bottom row, blue) coarse solver matrices for increasing number of cells. Each cell is discretized with 24 × 4 finite elements. (For interpretation of the references to color in this figure legend, the reader is referred to the web version of this article.)

This test shows that the reduction of the time-step size τ does not impair the performance of the GDSW solver, indicating that the bound in Theorem 1 might not be sharp in τ.

We show in Fig. 8 the solver performance over a time interval of $[0, 300]$ ms, simulating an heartbeat cycle. Except for a single peak in the EMI-GDSW condition number when the action potential is at rest (see Fig. 8 for its evolution in two different points of the considered domain), we observe that the EMI-GDSW is robust both in terms of condition number k_2 and number of linear iterations *it*, presenting lower values with respect to the AS and CG cases.

5.2.4. EMI-GDSW robustness varying the conductivity coefficients

This set of tests investigates the robustness of the EMI-GDSW solver with respect to heterogeneous distributions of intracellular diffusion coefficients σ_i, for $i = 1, \dots, N$. In particular, we consider three different distributions with $N = 8 \times 8$ cells, each discretized with 48 × 8 Q1 finite elements:

- `checkerboard` distribution, where the conductivities alternate between two values σ_i and $\sigma_i^\star$ in a checkerboard fashion;
- `capsule` distribution, where we include a inner square block of 4 × 4 cells with conductivity $\sigma_i^\star$, while in the surrounding cells the conductivity remain σ_i;
- `random` distribution, where we randomly generate for each cell the coefficient $\sigma_i^\star$.

The value $\sigma_i^\star$ is obtained by scaling σ_i by a factor α of 10^{-1}, 10^{-2}, 10^{-3} and 10^{-4}, except for the `random` setting, where $\sigma_i^\star = (\text{scaling factor}) \times (\sigma_i + n_{\text{rand}})$, with n_{rand} a randomly generated number between 0 and 10^{-3} (in order to perturb σ_i of a value with the same order of magnitude). In Figs. 9 and 10, we report three different time snapshots for each distribution, and also include for comparison the homogeneous distribution (`normal`) with $\sigma_i = 3 \times 10^{-3}$ in all cells.

Fig. 11(a) reports both condition number (k_2) and number of linear iterations (*it*) at $t = 5$ ms, while the boxplot in Fig. 11(b) shows the distribution of several tests related to the `random` case. The results show the robustness of EMI-GDSW, since k_2 and *it* remain fairly unchanged, with only a slight decrease in the former when reducing $\sigma_i^\star$. This is to be expected, since decreasing the diffusion coefficient $\sigma_i^\star$ and considering enough modified subdomains, the mass term with the potential jump would prevail.

6. Conclusions

We have designed a generalized Dryja–Smith–Widlund (GDSW) preconditioner for the solution of composite Discontinuous Galerkin discretizations of parabolic reaction–diffusion problems, where the solution can present discontinuities across the domain.

H/h	N_{dof}	EMI-GDSW		AS		CG	
		k_2	it	k_2	it	k_2	it
12	984	54.3	34	313.6	43	2.26e+03	118
18	1936	73.3	39	473.7	51	4.31e+03	160
24	3200	90.1	43	632.4	58	7.09e+03	204
30	4776	103.7	46	791.5	63	1.05e+04	246
36	6664	118.1	49	945.1	68	1.47e+04	288
42	8864	130.8	50	1.10e+03	73	1.92e+04	326
48	11376	143.8	52	1.26e+03	77	2.46e+04	365
54	14200	148.3	54	1.41e+03	80	3.10e+04	405
60	17336	163.2	56	1.57e+03	83	3.79e+04	443

(a) Condition number (k_2) and linear iterations (it) at final time $t = 5$ ms for EMI-GDSW (left), AS (center), unpreconditioned CG (right).

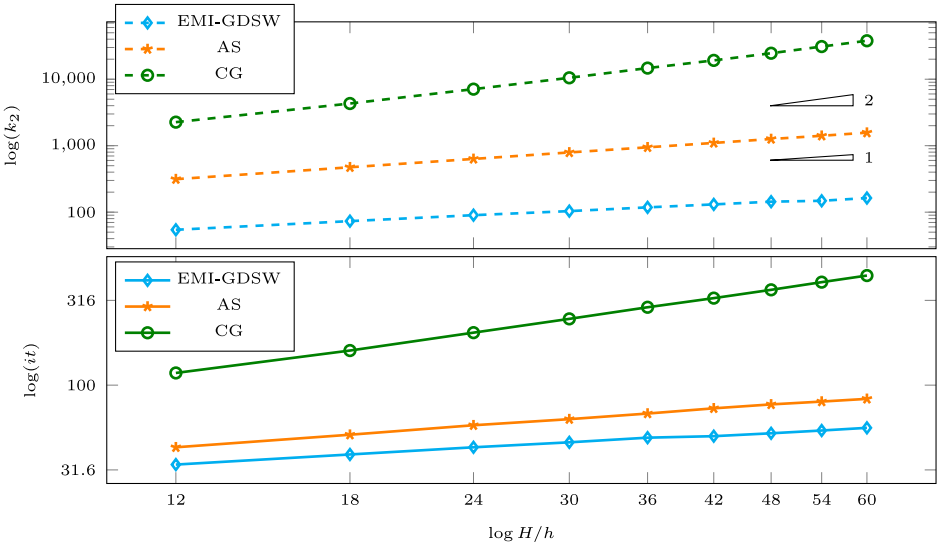

(b) Plots of condition number (k_2) and linear iterations (it) from the Table a) above.

Fig. 6. *EMI-GDSW optimality tests* on $[0, 5]$ ms. Condition number k_2 and linear iterations (it) at the final time $t = 5$ ms. Fixed time-step size $\tau = 0.05$ and number of 4×4 cells, each discretized with increasing number of finite elements.

These situations arise naturally, for instance, in the context of microscopic biomechanics modeling or in multiscale problems where model order-reduction techniques lead to face coupling of different dimensionalities. We mathematically prove a scalable (i.e. independent of the number of subdomains $N + 1$) and quasi-optimal (i.e. polylogarithmic in the ratio H/h) convergence rate bound for the proposed GDSW preconditioner, which depends on the time-step size and the magnitude of the diffusion coefficients. Extensive two-dimensional numerical tests confirm this theoretical result for the solution of the cardiac EMI reaction–diffusion model. Possible future work should address the extension of this result to the three-dimensional setting as well as larger overlaps, while investigating the design and analysis of advanced GDSW variants based on adaptive, reduced and multilevel techniques in the challenging composite Discontinuous Galerkin framework required by the EMI and other multicompartment reaction–diffusion problems.

The comparison of the current GDSW preconditioner with the BDDC preconditioner, as introduced in our previous paper [24], shows that the coarse solver of GDSW is larger and less sparse than that of BDDC. Moreover, GDSW requires more iterations to achieve convergence. However, we believe that GDSW is easier to implement in parallel, and since it is an overlapping method, inexact local solvers may be more effective compared to the BDDC case. A fair comparison between the two solvers should be performed on parallel architectures, but this is beyond our current capabilities, so we reserve it for a future study.

τ	EMI-GDSW		AS		CG	
	k_2	it	k_2	it	k_2	it
0.005	130.7	57	9.32e+03	183	2.55e+05	630
0.01	127.5	57	8.33e+03	177	1.55e+05	627
0.02	122.1	56	7.25e+03	168	9.38e+04	584
0.05	112.2	54	5.87e+03	157	5.26e+04	494
0.1	132.3	54	3.10e+03	114	4.26e+04	468

(a) Condition number (k_2) and linear iterations (it) at final time $t = 5$ ms for EMI-GDSW (left), AS (center), unpreconditioned CG (right).

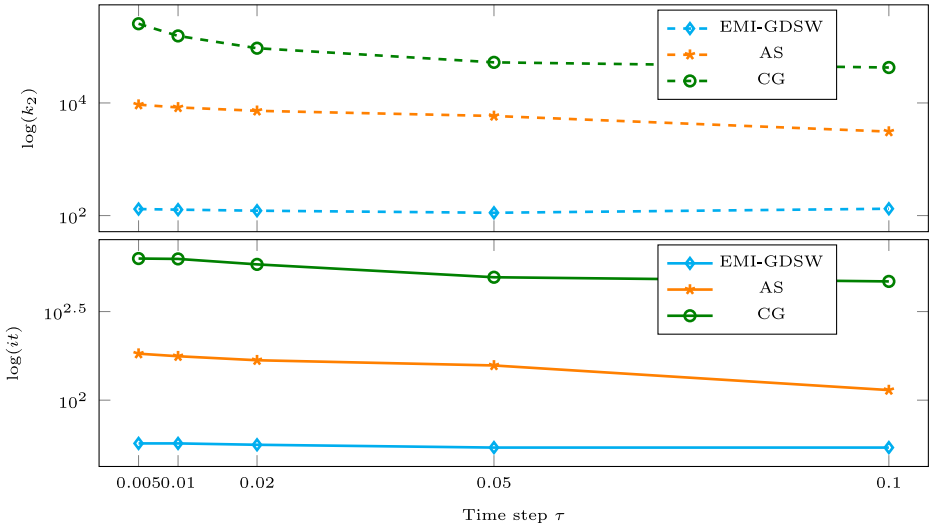

(b) Plots of condition number (k_2) and linear iterations (it) from the Table a) above.

Fig. 7. *EMI-GDSW dependence on the time-step size.* Condition numbers k_2 and linear iterations (it) at the final time $t = 5$ ms, when the time-step size τ is increased from 0.005 to 0.1. Fixed number of 12×12 cells, each discretized with 24×4 finite elements ($N_{\text{dof}} = 21440$).

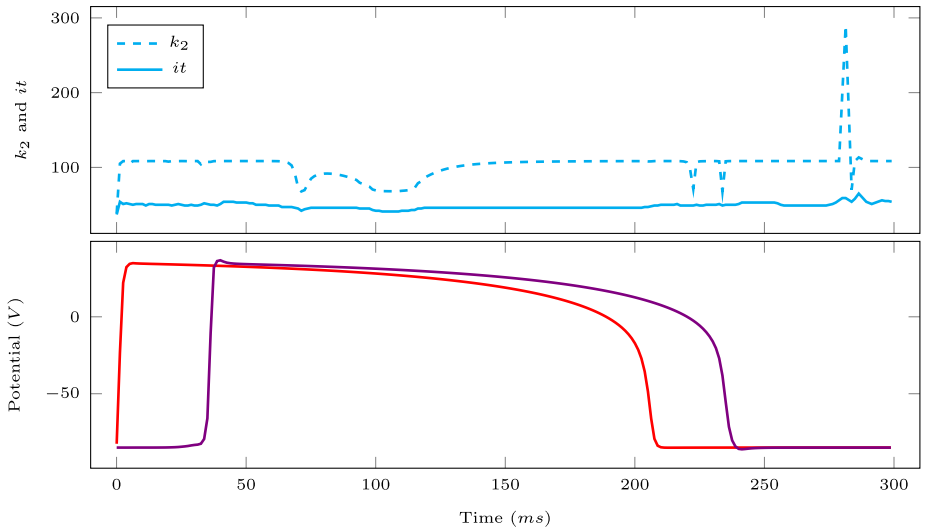

Fig. 8. Action potential propagation from two different points of the domain (bottom) and EMI-GDSW solver performance (top) over an heartbeat cycle of [0, 300] ms.

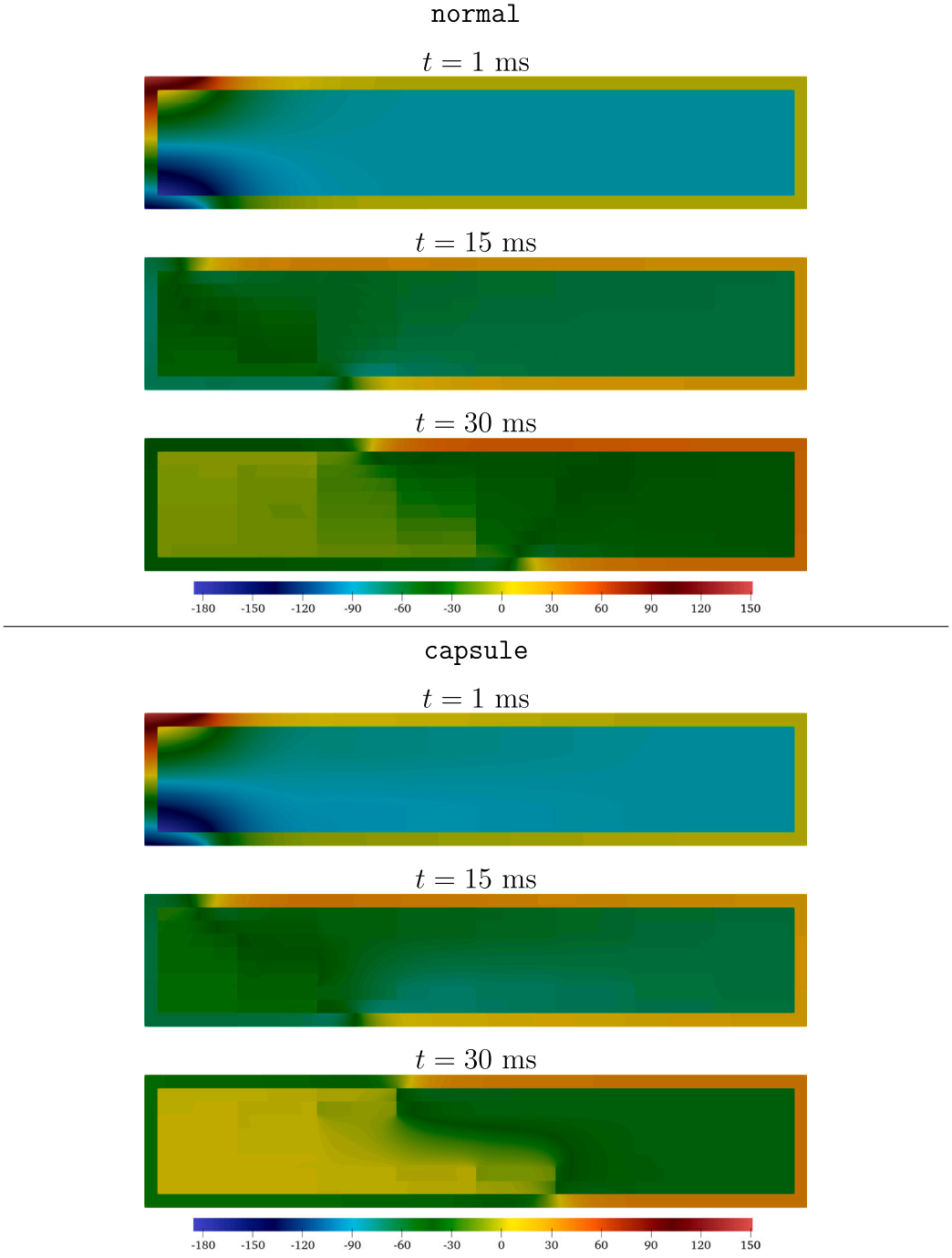

Fig. 9. Snapshots at times $t = 1, 15, 30$ ms of the EMI electric potentials for the `normal` distribution (top) with $\sigma_i = 3 \times 10^{-3}$ and the `capsule` distribution (bottom) with an inner block of 4×4 cells with $\sigma_i^\star = 10^{-4}\sigma_i$.

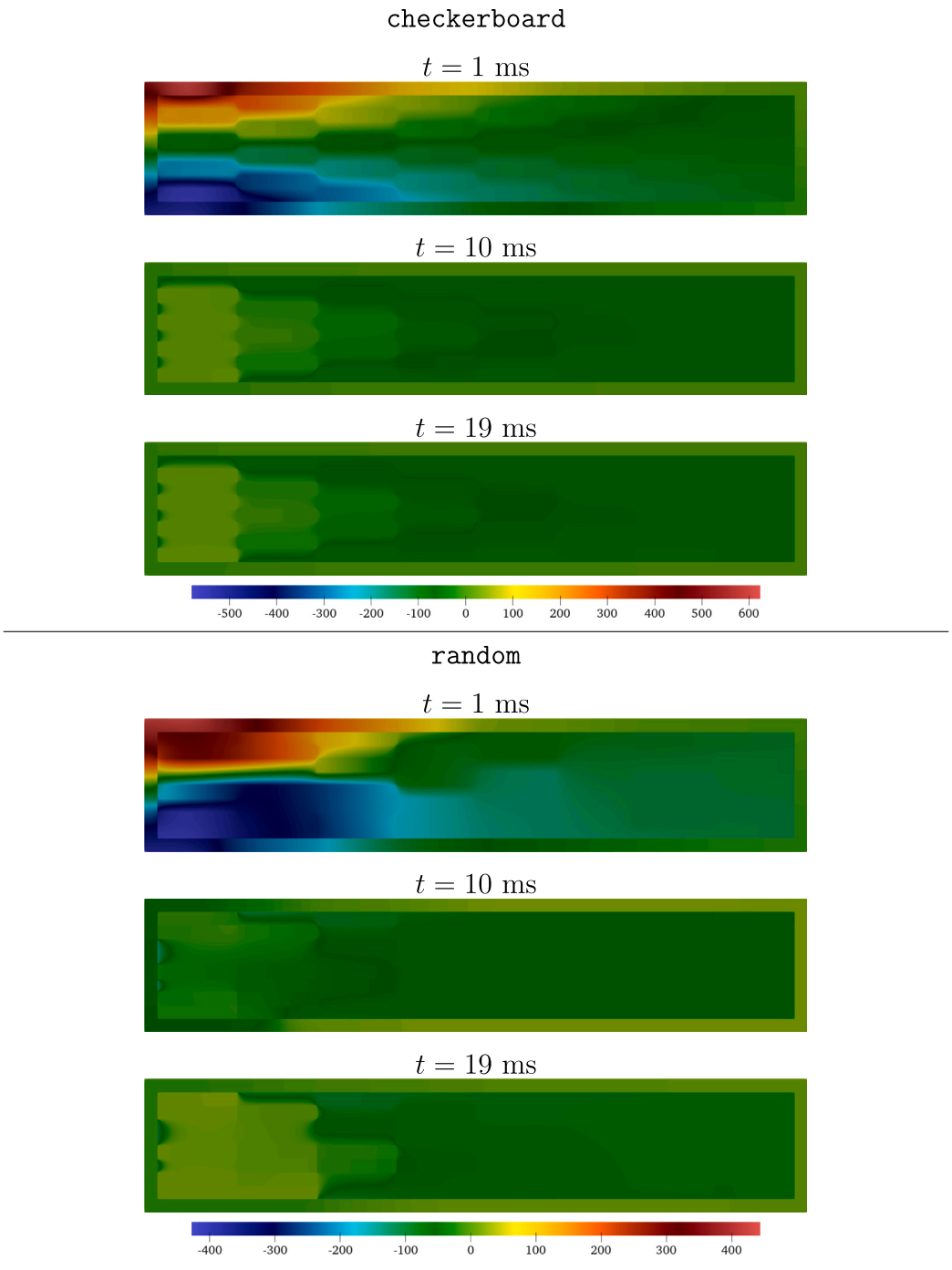

Fig. 10. Snapshots at times $t = 1, 10, 19$ ms of the EMI electric potentials for the `checkerboard` distribution (top) with checkerboard-like alternating cells with $\sigma_i^\star = 10^{-4}\sigma_i$ and `random` distribution (bottom) with $\sigma_i^\star = 10^{-4} \cdot (\sigma_i + n_{\text{rand}})$, where n_{rand} is randomly generated between 0 and 10^{-3}.

	α	1		10^{-1}		10^{-2}	
		k_2	it	k_2	it	k_2	it
`checkerboard`	$\sigma_i^\star = \alpha\sigma_i$	167.3	62	137.2	55	118.6	52
`capsule`		167.3	62	166.6	66	166.7	65
`random`	$\sigma_i^\star = \alpha \cdot (\sigma_i + n_{\text{rand}})$	-	-	172.90	64	162.89	63

	α	10^{-3}		10^{-4}	
		k_2	it	k_2	it
`checkerboard`	$\sigma_i^\star = \alpha\sigma_i$	117.3	53	117.2	54
`capsule`		167.8	65	164.4	65
`random`	$\sigma_i^\star = \alpha \cdot (\sigma_i + n_{\text{rand}})$	153.80	65	164.59	66

(a) Condition number (k_2) and linear iterations (it) at final time $t = 5$ ms for EMI-GDSW with three different distribution of conductivity coefficients σ_i. For the `random` distribution we report the average values over 10 experiments (it are rounded to the closest integer).

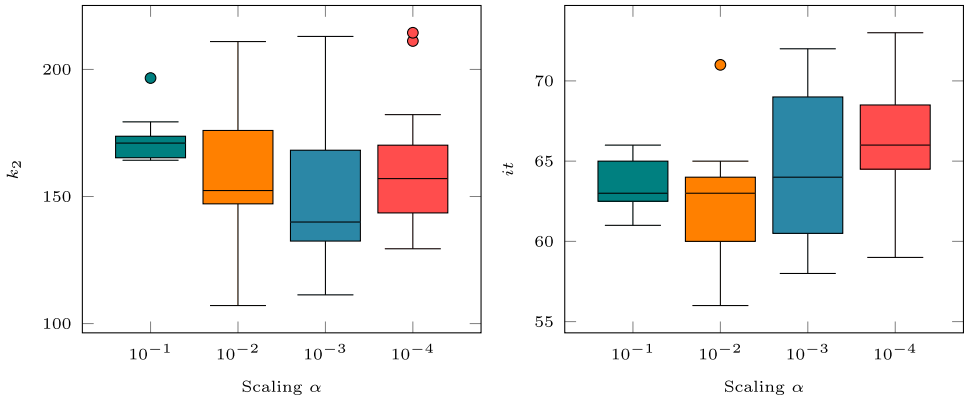

(b) Boxplots with the statistical distribution of the results (k_2 on the left and it on the right) related to 10 `random` cases with different scaling factors α. The horizontal lines correspond to the lower whisker (-1.5 the interquartile range), the median (0.5-quartile of data) and the upper whisker ($+1.5$ the interquartile range), while the colored circles are outliers.

Fig. 11. *EMI-GDSW robustness tests.* EMI-GDSW condition numbers k_2 and linear iterations (it) at time $t = 5$ ms with three different distributions (`checkerboard`, `capsule`, `random`) of the conductivity coefficients σ_i. Fixed time step $\tau = 0.05$ on the interval $[0, 5]$ ms. Fixed number of 8×8 cells, each discretized with 48×8 finite elements ($N_{\text{dof}} = 36576$). (For interpretation of the references to color in this figure legend, the reader is referred to the web version of this article.)

CRediT authorship contribution statement

Ngoc Mai Monica Huynh: Writing – original draft, Methodology, Formal analysis. **Luca F. Pavarino:** Writing – original draft. **Simone Scacchi:** Writing – original draft, Methodology, Formal analysis.

Declaration of competing interest

The authors declare that they have no known competing financial interests or personal relationships that could have appeared to influence the work reported in this paper.

Acknowledgments

The authors have been supported by the European High-Performance Computing Joint Undertaking EuroHPC under grant agreement No 955495 (MICROCARD) co-funded by the Horizon 2020 programme of the European Union (EU), and the Italian Ministry of Economic Development. All the authors are members of the Gruppo Nazionale Calcolo Scientifico-Istituto Nazionale di Alta Matematica (GNCS-INdAM). L.F.P. has been supported by MUR (PRIN 202232A8AN_002 and PRIN P2022B38NR_001) funded by European Union - Next Generation EU. S.S. has been supported by MUR (PRIN 202232A8AN_003 and PRIN P2022B38NR_002) funded by European Union - Next Generation EU.

Data availability

Data will be made available on request.

References

[1] M. Corti, P.F. Antonietti, L. Dedé, A.M. Quarteroni, Numerical modeling of the brain poromechanics by high-order discontinuous Galerkin methods, Math. Models Methods Appl. Sci. (2023) 1–33.

[2] E. Piersanti, J.J. Lee, T. Thompson, K.-A. Mardal, M.E. Rognes, Parameter robust preconditioning by congruence for multiple-network poroelasticity, SIAM J. Sci. Comput. 43 (2021) B984–B1007.

[3] K.H. Jaeger, A.G. Edwards, W.R. Giles, A. Tveito, From millimeters to micrometers; re-introducing myocytes in models of cardiac electrophysiology, Front. Physiol. 12 (2021) 763584.

[4] A. Tveito, et al., A cell-based framework for numerical modeling of electrical conduction in cardiac tissue, Front Phys 5 (2017) 48.

[5] A. Tveito, K.-A. Mardal, M.E. Rognes, Modeling excitable tissue - the EMI Framework, Simula Springer Briefs in Comput 7 (2021).

[6] M. Corti, P.F. Antonietti, F. Bonizzoni, L. Dedé, A. Quarteroni, Discontinuous Galerkin methods for Fisher-Kolmogorov equation with application to α-synuclein spreading in Parkinson's disease, Comp. Methods Appl. Mech. Eng. 417 (2023) 116450.

[7] G. Kanschat, Preconditioning methods for local discontinuous Galerkin discretizations, SIAM J. Sci. Comput. 25 (3) (2003) 815–831.

[8] V.A. Dobrev, R.D. Lazarov, P.S. Vassilevski, L.T. Zikatanov, Two-level preconditioning of discontinuous Galerkin approximations of second-order elliptic equations, Numer. Linear Algebra Appl. 13 (9) (2006) 753–770.

[9] B. Ayuso de Dios, M. Holst, Y. Zhu, L. Zikatanov, Multilevel preconditioners for discontinuous Galerkin approximations of elliptic problems with jump coefficients, Math. Comp. 83 (287) (2014) 1083–1120.

[10] B. Ayuso de Dios, L. Zikatanov, Uniformly convergent iterative methods for discontinuous Galerkin discretizations, J. Sci. Comput. 40 (2009) 4–36.

[11] E. Centofanti, N.M.M. Huynh, L.F. Pavarino, S. Scacchi, Multigrid solvers on GPUs for the cardiac EMI model, 2024, (in preparation).

[12] P.F. Antonietti, B. Ayuso, Schwarz domain decomposition preconditioners for discontinuous Galerkin approximations of elliptic problems: non-overlapping case, ESAIM Math. Model. Numer. Anal. 41 (1) (2007) 21–54.

[13] P.F. Antonietti, B. Ayuso, Multiplicative Schwarz methods for discontinuous Galerkin approximations of elliptic problems, ESAIM Math. Model. Numer. Anal. 42 (3) (2008) 443–469.

[14] C. Canuto, L.F. Pavarino, A.B. Pieri, BDDC preconditioners for continuous and discontinuous Galerkin methods using spectral/hp elements with variable local polynomial degree, IMA J. Numer. Anal. 34 (3) (2014) 879–903.

[15] M. Dryja, J. Galvis, M. Sarkis, A FETI-DP preconditioner for a composite finite element and discontinuous Galerkin method, SIAM J. Numer. Anal. 51–1 (2013) 400–422.

[16] M. Dryja, J. Galvis, M. Sarkis, A deluxe FETI-DP preconditioner for a composite finite element and DG method, Comput. Methods Appl. Math. 15 (4) (2015) 465–482.

[17] A. Budisa, X. Hu, M. Kuchta, K.-A. Mardal, L.T. Zikatanov, Algebraic multigrid methods for metric-perturbed coupled problems, SIAM J. Sci. Comput. 46 (3) (2024) A1461–A1486.

[18] P. Benedusi, P. Ferrari, M. Rognes, S. Serra-Capizzano, Modeling excitable cells with the EMI equations: spectral analysis and iterative solution strategy, J. Sci. Comput. 98 (2024) 58.

[19] P. Benedusi, P. Ferrari, M. Causemann. S. Serra-Capizzano, Dense cell-by-cell systems of PDEs: approximation, spectral analysis, and preconditioning, 2024, arXiv preprint arXiv:2409.13432.

[20] N.M.M. Huynh, F. Chegini, L.F. Pavarino, M. Weiser, S. Scacchi, Convergence analysis of BDDC preconditioners for composite DG discretizations of the cardiac cell-by-cell model, SIAM J. Sci. Comput. 45 (6) (2023) A2836–A2857.

[21] F. Chegini, A. Frohely, N.M.M. Huynh, L.F. Pavarino, M. Potse, S. Scacchi, M. Weiser, Efficient numerical methods for simulating cardiac electrophysiology with cellular resolution, in: 10th Edition of the International Conference on Computational Methods for Coupled Problems in Science and Engineering, 2023.

[22] S. Balay, et al., PETSc web page, 2022, https://petsc.org/.

[23] C.R. Dohrmann, A. Klawonn, O.B. Widlund, Domain decomposition for less regular subdomains: overlapping Schwarz in two dimensions, SIAM J. Numer. Anal. 46 (4) (2008) 2153–2168.

[24] A. Heinlein, A. Klawonn, S. Rajamanickam, O. Rheinbach, Frosch: a fast and robust overlapping Schwarz domain decomposition preconditioner based on xpetra in trilinos, in: Domain Decomposition Methods in Science and Engineering XXV (DD 2018), in: Lecture Notes in Computational Science and Engineering, vol 138, Springer, Cham.

[25] A. Heinlein, A. Klawonn, J. Knepper, O. Rheinbach, Adaptive GDSW coarse spaces for overlapping Schwarz methods in three dimensions, SIAM J. Sci. Comput. 41 (5) (2019) A3045–A3072.

[26] A. Heinlein, A. Klawonn, J. Knepper, O. Rheinbach, O. Widlund, Adaptive GDSW coarse spaces of reduced dimension for overlapping Schwarz methods, SIAM J. Sci. Comput. 44 (3) (2022) A1176–A1204.

[27] A. Heinlein, O. Rheinbach, F. Röver, A multilevel extension of the GDSW overlapping Schwarz preconditioner in two dimensions, Comput. Methods Appl. Math. 23 (4) (2023) 953–968.

[28] N.M.M. Huynh, L.F. Pavarino, S. Scacchi, Parallel Newton–Krylov BDDC and FETI-DP Deluxe Solvers for Implicit Time discretizations of the Cardiac Bidomain Equations, SIAM J. Sci. Comput. 44 (2) (2022) B224–B249.

[29] N.M.M. Huynh, Newton-Krylov-BDDC deluxe solvers for non-symmetric fully implicit time discretizations of the Bidomain model, Numer. Math. 152 (4) (2022) 841–879.

[30] A. Toselli, O.B. Widlund, Domain Decomposition Methods, Algorithms and Theory, Springer, 2005.

[31] K.H. Jaeger, K.G. Hustad, X. Cai, A. Tveito, et al., Efficient numerical solution of the EMI model representing the extracellular space (E), cell membrane (M) and intracellular space (I) of a collection of cardiac cells, Front. Phys 8 (2021).

[32] P. Colli Franzone, L.F. Pavarino, S. Scacchi, Mathematical Cardiac Electrophysiology, vol. 13, Springer, 2014.

[33] M. Fedele, R. Piersanti, F. Regazzoni, M. Salvador, P.C. Africa, M. Bucelli, A. Zingaro, L. Dede', A. Quarteroni, A comprehensive and biophysically detailed computational model of the whole human heart electromechanics, Comp. Meth. App. Math. Engrg. 410 (2023) 115983.

[34] L. Tung, (Ph.D. thesis), M.I.T. Cambridge, Mass., 1978.

[35] M. Veneroni, Reaction–diffusion systems for the macroscopic bidomain model of the cardiac electric field, Nonlinear Anal. Real World Appl. 10 (2) (2009) 849–868.

[36] P.C. Africa, M. Salvador, P. Gervasio, L. Dedé, A. Quarteroni, A matrix–free high-order solver for the numerical solution of cardiac electrophysiology, J. Comput. Phys. 478 (2023) 111984.

[37] N.A. Barnafi, N.M.M. Huynh, L.F. Pavarino, S. Scacchi, Robust parallel nonlinear solvers for implicit time discretizations of the bidomain equations with staggered ionic models, Comput. Math. Appl. 167 (2024) 134–149.
[38] E. Centofanti, S. Scacchi, A comparison of algebraic multigrid bidomain solvers on hybrid CPU–GPU architectures, Comp. Methods Appl. Mech. Eng. 423 (2024) 116875.
[39] F. Chegini, T. Steinke, M. Weiser, Efficient adaptivity for simulating cardiac electrophysiology with spectral deferred correction methods, 2023, arXiv preprint arXiv:2311.07206.
[40] G. Plank, M. Liebmann, R. Weber dos Santos, E. Vigmond, G. Haase, Algebraic multigrid preconditioner for the cardiac bidomain model, IEEE Trans. Biomed. Eng. 54 (4) (2007) 585–596.
[41] E.J. Vigmond, R. Weber dos Santos, A.J. Prassl, M. Deo, G. Plank, Solvers for the cardiac bidomain equations, Progr Biophys. Molec. Biol. 96 (1–3) (2008) 3–18.
[42] M. Weiser, F. Chegini, Adaptive multirate integration of cardiac electrophysiology with spectral deferred correction methods, in: P. Nithiarasu, C. Vergara (Eds.), CMBE22–7th International Conference on Computational & Mathematical Biomedical Engineering, 2022, pp. 528–531.
[43] S. Rohr, Role of gap junctions in the propagation of the cardiac action potential, Cardiov. Res. 62 (2) (2004) 309–322.
[44] G. Rosilho de Souza, R. Krause, S. Pezzuto, Boundary integral formulation of the cell-by-cell model of cardiac electrophysiology, Eng. Anal. Bound. Elem. 158 (2024) 239–251.
[45] R.R. Aliev, A.V. Panfilov, A simple two-variable model of cardiac excitation, Chaos Solitons Fractals 7 (3) (1996) 293–301.
[46] C.R. Dohrmann, O.B. Widlund, An overlapping Schwarz algorithm for almost incompressible elasticity, SIAM J. Numer. Anal. 47 (4) (2009) 2897–2923.